



## Article

# Photocatalytic Performance of ZnO-Graphene Oxide Composites towards the Degradation of Vanillic Acid under Solar Radiation and Visible-LED

Neda Mirikaram <sup>1,2,†</sup>, Álvaro Pérez-Molina <sup>1,†</sup>, Sergio Morales-Torres <sup>1</sup>, Amir Salemi <sup>2</sup>,  
Francisco J. Maldonado-Hódar <sup>1</sup> and Luisa M. Pastrana-Martínez <sup>1,\*</sup>

<sup>1</sup> Department of Inorganic Chemistry, Faculty of Sciences, University of Granada, Avda. Fuente Nueva s/n, ES-18071 Granada, Spain; mirikaram@gmail.com (N.M.); alpemo@ugr.es (Á.P.-M.); semoto@ugr.es (S.M.-T.); fjmalon@ugr.es (F.J.M.-H.)

<sup>2</sup> Environmental Sciences Research Institute, Shahid Beheshti University, Tehran 19839-63113, Iran; a\_salemi@sbu.ac.ir

\* Correspondence: lpastrana@ugr.es; Tel.: +34-(958)-248-489

† The authors contributed equally to this study.

**Abstract:** Graphene oxide (GO) is used to enhance the photocatalytic activity of ZnO nanoparticles for the degradation of vanillic acid (VA) under simulated solar light and visible-LED ( $\lambda > 430$  nm). ZnO-GO composites are prepared by a mixing and sonication process with different GO loadings (i.e., from 1.8 to 6.5 wt.%). The materials are extensively characterized by thermogravimetric analysis (TGA), physisorption of N<sub>2</sub>, X-ray diffraction (XRD), infrared spectroscopy (FTIR), scanning electron microscopy (SEM), point of zero charge (pH<sub>PZC</sub>), and UV-Vis diffuse reflectance spectroscopy (DRUV). The presence of GO increases the photocatalytic activity of all the prepared composites in comparison with the pristine ZnO. The highest photocatalytic activity is found for the composite containing 5.5 wt.% of GO (i.e., ZnO-GO5.5), reaching a VA degradation of 99% and 35% under solar light and visible-LED, respectively. Higher TOC removal/VA degradation ratios are obtained from the experiments carried out under visible-LED, indicating a more effective process for the mineralization of VA than those observed under simulated solar light. The influence of hole, radical, and non-radical scavengers is studied in order to assess the occurrence of the reactive oxygen species (ROS) involved in the photocatalytic mechanism. The study of the photo-stability during three reuse experiments indicates that the presence of GO in the composites reduces the photocorrosion in comparison with pristine ZnO.

**Keywords:** graphene oxide; ZnO; vanillic acid; water treatment; scavengers



**Citation:** Mirikaram, N.; Pérez-Molina, Á.; Morales-Torres, S.; Salemi, A.; Maldonado-Hódar, F.J.; Pastrana-Martínez, L.M. Photocatalytic Performance of ZnO-Graphene Oxide Composites towards the Degradation of Vanillic Acid under Solar Radiation and Visible-LED. *Nanomaterials* **2021**, *11*, 1576. <https://doi.org/10.3390/nano11061576>

Academic Editor: Vincenzo Vaiano

Received: 27 April 2021

Accepted: 11 June 2021

Published: 15 June 2021

**Publisher's Note:** MDPI stays neutral with regard to jurisdictional claims in published maps and institutional affiliations.



**Copyright:** © 2021 by the authors. Licensee MDPI, Basel, Switzerland. This article is an open access article distributed under the terms and conditions of the Creative Commons Attribution (CC BY) license (<https://creativecommons.org/licenses/by/4.0/>).

## 1. Introduction

Over the past 40 years, advanced oxidation processes (AOPs) have been successfully applied to manage the problematic issues associated to water, air, and soil pollution [1]. These processes are mainly based on the generation of hydroxyl radicals (HO•) which can generate a sequence of reactions capable of degrading contaminants into CO<sub>2</sub> and H<sub>2</sub>O, or converting them into less toxic organic compounds. These processes include heterogeneous photocatalysis, which is based on the effective utilization of ultraviolet (UV) or solar irradiation as a technology for environmental applications [2]. On the other hand, many structural materials including polymers, metals, ceramics, glasses, and composite materials have been synthesized for different industrial applications [3–8].

Normally, metal oxides such as titanium dioxide (TiO<sub>2</sub>), zinc oxide (ZnO), zirconia (ZrO<sub>2</sub>), tungsten trioxide (WO<sub>3</sub>), and vanadium oxide (V<sub>2</sub>O<sub>5</sub>), have been used as semiconductor photocatalysts for water and air decontamination, as well as for energy applications [9–12]. ZnO is an n-type semiconductor with a band gap ca. 3.22 eV and a large excitation binding energy of ca. 60 meV. It can be considered as a suitable successor of

the benchmark TiO<sub>2</sub> semiconductor due to its similar properties such as strong oxidation ability, good photocatalytic properties, chemical stability, biocompatibility, non-toxicity, high photosensitivity, and electronic and piezoelectric properties, among others [13–15]. This semiconductor usually exists in one-dimensional (1D), two-dimensional (2D) and three-dimensional (3D) associations [16], and has been used in a wide range of applications, such as sensors [17], photocatalysis [14,18–21], transistors, solar cells [22,23], etc. It is well known that the use of ZnO in photocatalysis displays some drawbacks such as: (i) the limitation of its use in the visible range due to its wide band gap [24]; (ii) particle aggregation during photocatalytic reactions which significantly restrict the photocatalytic activity of ZnO at a large scale [25]; and (iii) the rapid recombination of the photogenerated electron-hole pairs [26,27].

Many strategies have been carried out to improve the photocatalytic performance of ZnO, e.g., the design of suitable sizes and morphologies [28,29], noble metal loading [14,30,31], heteroatom doping [32–34], or by forming semiconductor composites [35], among others. In particular, the design and development of hybrids based on the coupling of carbon materials and ZnO is an effective option for enhancing its photocatalytic response under UV/Vis irradiation [18,36–38], by inhibiting the electron-hole recombination as well as extending the light absorption into visible range [39].

Amongst the vast number of carbon nanomaterials, graphene and its derivatives have been shown to significantly enlarge the photocatalytic degradation activity of ZnO in the field of photocatalytic wastewater treatment [37,40–43]. Of particular interest is the use of one of the most well-known derivatives of graphene, i.e., graphene oxide (GO), for the synthesis of ZnO-GO hybrid materials, as the presence of oxygen-containing surface groups in GO offers an excellent dispersibility in polar solvents for the synthesis of the composites. Furthermore, GO can improve the photocatalytic efficiency in the composites by: (i) acting as an electron-acceptor, hindering the electron-hole recombination; (ii) increasing the adsorption of organic pollutants through  $\pi$ - $\pi$  interactions between the  $sp^2$  region of graphene and the aromatic pollutant; and (iii) creating oxygen vacancies in the lattice of ZnO, extending its response under the visible light region [35,37,42,44,45]. Various methods have been reported for the synthesis of ZnO-GO composites, such as hydrothermal process [46,47], chemical vapor deposition (CVD) [35,48,49], physical vapor deposition (PVD) [50,51], pulsed laser deposition (PLD) [52], spray pyrolysis [53,54], solvothermal [19], and microwave synthesis [55], among others.

In this paper, we report a low-cost and scaling up method for the synthesis of ZnO-GO composites. Nanostructured ZnO particles were formed using zinc acetate as precursor, then the composites were synthesized by a simple mixing and sonication method. The photocatalytic performance of the prepared materials was tested in the degradation of a phenolic compound, namely vanillic acid (VA), under both simulated solar irradiation and visible-LED ( $\lambda > 430$  nm). VA is a model compound typically present in the phenolic fractions of olive mill wastewater (OMW). The presence of this phenolic compound constitutes an important environmental problem, especially in Mediterranean countries and, in particular, areas of southern Spain, where a great number of plants are involved in the production and refining of olive oil [56].

## 2. Materials and Methods

### 2.1. Synthesis of GO, ZnO and ZnO-GO Composites

Graphite oxide was prepared using a modified Hummers' method [57,58]. Specifically, 5 g of graphite (powder < 20  $\mu$ m, Sigma-Aldrich, St. Louis, MO, USA) and 5 g of sodium nitrate, NaNO<sub>3</sub> (99.0%, Acros Organics, Geel, Belgium) were put into 240 mL of concentrated sulfuric acid, H<sub>2</sub>SO<sub>4</sub> (96–99%, supplied by PanReac AppliChem, Darmstadt, Germany). The mixture was kept stirring for 30 min in an ice bath to prevent the temperature exceeding 10 °C. Thereafter, 30 g of potassium permanganate, KMnO<sub>4</sub> (99.0%, PanReac AppliChem, Darmstadt, Germany) was added gradually with stirring (30 min). The ice bath was then removed, and the mixture was warmed at 35 °C and stirred for 24 h.

The reaction was terminated by slowly adding 800 mL of distilled water and 30 mL of 30% hydrogen peroxide, H<sub>2</sub>O<sub>2</sub> (30% w/w, PanReac AppliChem, Darmstadt, Germany) solution. Finally, the resulting dispersion was filtered and washed repeatedly with distilled water until its pH became neutral. The acquired solid (i.e., graphite oxide) was dried in an oven at 60 °C. Graphene oxide (GO) was prepared by sonication in an aqueous solution using an ultrasound bath (ultrasonic processor UP400S, 24 kHz, Hielscher, Germany). The undissolved solid was removed by centrifugation for 30 min at 3000 rpm to obtain the GO suspension (1 g L<sup>-1</sup>).

ZnO nanoparticles were prepared by calcination of zinc acetate dihydrate, Zn(Ac)<sub>2</sub>·2H<sub>2</sub>O (≥99.0%, Alfa Aesar, Haverhill, MA, USA) in a furnace with air flow at 5 °C min<sup>-1</sup> until 600 °C, with a soak time of 3 h [59]. ZnO-GO composites were synthesized by a sonication method [38,60]. Briefly, the required amount of ZnO was added to different amounts of an aqueous GO dispersion (1 g L<sup>-1</sup>) and ethanol (96% v/v) mixture in a proportion of 1:2, respectively. The resulting dispersion was kept under vigorous agitation for 30 min, then sonicated for 2 h in an ultrasound bath (ultrasonic processor UP400S, 24 kHz, Hielscher, Germany). The obtained composites were filtered, washed with ultrapure water, and dried at 120 °C in a vacuum oven for 8 h. The GO loading was fitted at ca. 2, 3, 5, and 7 wt.%.

## 2.2. Characterization Techniques

Infrared spectra (ATR-IR) were recorded in a NICOLET 510P spectrometer (Thermo Fisher Scientific, Waltham, MA, USA) with an attenuated total reflection accessory and a ZeSn as ATR crystal. Thermogravimetric (TG) analysis of the composites was obtained using a SHIMADZU TGA-50H thermobalance (Shimadzu Corporation, Japan) by heating the sample in air flow up to 950 °C with a heating rate of 20 °C min<sup>-1</sup>. The N<sub>2</sub> adsorption-desorption isotherms at -196 °C were obtained using a Quadrasorb SI equipment (Quantachrome, Boston Beach, FL, USA). The samples were outgassed overnight at 110 °C under high vacuum (10<sup>-6</sup> mbar). The Brunauer-Emmett-Teller (BET) equation was applied to calculate the apparent surface area (S<sub>BET</sub>) [61,62], while the mesopore volume (V<sub>meso</sub>) and total pore volume (V<sub>total</sub>) were determined by applying the Barrett, Joyner, and Halenda (BJH) method [63,64] to the desorption branch of the N<sub>2</sub> isotherms. The point of zero charge (pH<sub>PZC</sub>) of the materials was determined following the method described elsewhere [65,66]. The surface morphology of the synthesized photocatalysts was investigated by scanning electron microscopy (SEM) using a LEO (Carl Zeiss) GEMINI-1430-VP microscope (Oberkochen, Germany). Transmission electron microscopy (HRTEM) images were taken using a FEI Titan G2 60-300 microscope (FEI, Hillsboro, OR, USA) with a high brightness electron gun (X-FEG) operated at 300 kV and equipped with a Cs image corrector (CEOS). The X-ray diffraction (XRD) patterns were obtained using a Philips PW 1710 diffractometer (Bruker, Rivas-Vacia, Madrid, Spain) provided with a CuK $\alpha$  radiation and a nickel filter that removes  $\kappa\beta$  radiation. The average crystal size (D) of the samples was calculated by the Scherrer formula [67]:

$$D = \frac{0.94\lambda}{\beta \cos\theta} \quad (1)$$

where  $\lambda$  is the wavelength of the X-ray,  $\beta$  is the FWHM (full-width at half-maximum) and  $\theta$  is the diffraction angle. X-ray photoelectron spectroscopy (XPS) measurements were carried out using a Physical Electronics VersaProbe II apparatus (PHI, Chanhassen, MN, USA) equipped with a MgK $\alpha$  X-ray source ( $h\nu = 1486.6$  eV) operating at 1.3 V and 20 mA, and a hemispherical electron analyzer. Survey and multi-region spectra were recorded at the O1s and Zn2p photoelectron peaks. The optical properties of the photocatalysts were characterized by a UV-Vis spectrophotometer CARY 5E (VARIAN, Palo Alto, California, USA) equipped with a diffuse reflectance accessory (DRA). The band gap of the materials was calculated from the corresponding Tauc plots using  $(\text{Abs}\cdot h\nu)^{1/2}$  units as a function of energy (eV).

### 2.3. Photocatalytic Tests

The photocatalytic performance of the prepared catalysts was evaluated for the degradation of vanillic acid, VA ( $C_8H_8O_4$ , 97%, Sigma-Aldrich, St. Louis, MO, USA) in aqueous solutions under both simulated solar irradiation and visible-LED at room temperature (average 25 °C). Solar irradiation was carried out using a SOLAR BOX 1500e (CO.FE.MEGRA, Milano, Italy) with a 1500 W Xenon lamp ( $500 \text{ W m}^{-2}$  of irradiance power). Irradiation with visible light was performed with an LED lamp from Oriel, model LSH-7320 LED Solar Simulator (Metrohm, Herisau, Switzerland), with a total power output of  $110 \text{ mW cm}^{-2}$  and a wavelength range from 410 to 1100 nm.

The photocatalytic experiments were performed in a glass reactor loaded with 50 mL of solution containing the model pollutant VA ( $20 \text{ mg L}^{-1}$ ). The composite concentration was fixed as  $1 \text{ g L}^{-1}$  to avoid the effect of light scattering. The suspension was magnetically stirred and continuously purged with an oxygen flow. A dark period (30 min) was maintained before switching on the lamp in order to achieve the adsorption–desorption equilibrium conditions.

A syringe polyethersulfone (PES) filter of  $0.45 \mu\text{m}$  (Agilent Technologies, CA, USA) was used to separate the photocatalyst from the solution. The concentration of VA was determined by Ultra High-Performance Liquid Chromatography (UHPLC), using a Shimadzu Corporation apparatus (model Nexera, Tokyo, Japan) equipped with a Pump LC-30AD, an Autosampler SIL-30AC, an Oven CTO-20AC, a Degasser DGU-20A5r, a System Controller CBM-20 A Lite, and a Diode Array Detector (SPD-M20A). Chromatographic separation was optimized using a Shim-pack GISS-HP C18  $3 \mu\text{m}$  column ( $100 \times 3.0 \text{ mm I.D.}$ ) supplied by Shimadzu Corporation (Tokyo, Japan). The temperature of the column oven and autosampler were set at 40 °C and 15 °C, respectively, while the injection volume was 20  $\mu\text{L}$ . The mobile phase consisted of a mixture of acetonitrile, water, and acetic acid (29:70:1), respectively, at isocratic conditions and with a flow rate of  $1 \text{ mL min}^{-1}$ .

The total organic carbon (TOC) content of initial and final samples was determined at the end of the experiments (i.e., 60 and 180 min for simulated solar light and visible-LED, respectively) using a TOC-5000A apparatus (Shimadzu, Kyoto, Japan).

The photocatalytic degradation was calculated using the following equation:

$$[VA] = [VA]_0 \times e^{-k_{ap} \times t} \quad (2)$$

where  $k_{ap}$  is the pseudo–first order kinetic constant,  $t$  is the reaction time, and  $[VA]_0$  and  $[VA]$  denote the pollutant concentration at  $t = 0$  and  $t = t$ , respectively. The values of  $k_{ap}$  were obtained by non–linear regression.

The photocatalytic degradation pathway of VA was studied using ethylenediaminetetraacetic acid (EDTA, 1.0 mM), furfuryl alcohol (FFA, 1.0 mM), and methanol (MeOH, 1.0 mM) and as hole, singlet oxygen ( $^1O_2$ ), and radical scavengers, respectively [58].

## 3. Results and Discussion

### 3.1. Materials Characterization

The GO content in the composites was verified by thermogravimetric analysis (TG). Figure 1 shows the thermogravimetric analysis (TG) under air flow for GO and ZnO, as well as for the composites. The GO content of the composites was determined by burning in TG experiments, which directly analyze the weight loss along the combustion of GO in the composite (Figure 1). The results indicate a weight loss of 1.8, 2.8, 5.5, and 6.5 wt.% which is in agreement with the nominal GO content of the composites (i.e., 2.0, 3.0, 5.0, and 7.0 wt.%, respectively). Taking into account the obtained weight loss, the composites were labelled as ZnO-GO1.8, ZnO-GO2.8, ZnO-GO5.5, and ZnO-GO6.5 for GO loading of 1.8, 2.8, 5.5 and, 6.5 wt.%, respectively. For GO, the weight loss observed up to ca. 500 °C should be attributed to the removal of oxygenated surface groups of GO, followed by the carbon combustion, as previously reported in the literature. [58,68]. Regarding the TG of composites, the carbon combustion occurs at lower temperatures (i.e., <500 °C). These

results suggest that the presence of ZnO in the composites could have a catalytic effect on the combustion of the GO.

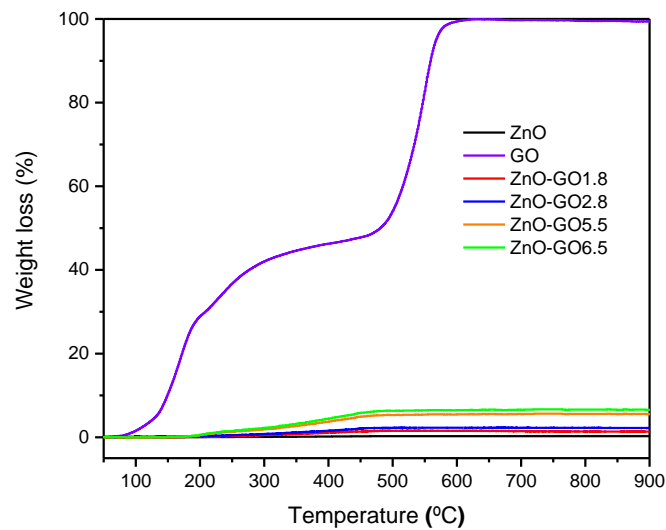


**Figure 1.** Thermogravimetric analysis in air of GO, pristine ZnO, ZnO-GO1.8, ZnO-GO2.8, ZnO-GO5.5, and ZnO-GO6.5 composites.

The textural characterization of pristine ZnO and the corresponding composites was studied by physisorption of  $N_2$  at  $-196^\circ C$ . Figure 2 shows the  $N_2$  adsorption-desorption isotherms of the prepared materials. In general, the isotherms can be classified as type-II, in accordance with IUPAC classification. These results indicate the samples consist of macroporous materials, or materials with a low porosity [60]. In fact, the  $N_2$  volume is negligible as a consequence of the absence of micropores at a very low relative pressure. However, a large amount of  $N_2$  is adsorbed at high relative pressures due to the presence of large mesopores. In addition, all isotherms presented a small hysteresis loop of type H3, typical of agglomerates formed by platelets or adsorbents with slit-shaped pores, which could correspond to GO layers coated by ZnO particles.

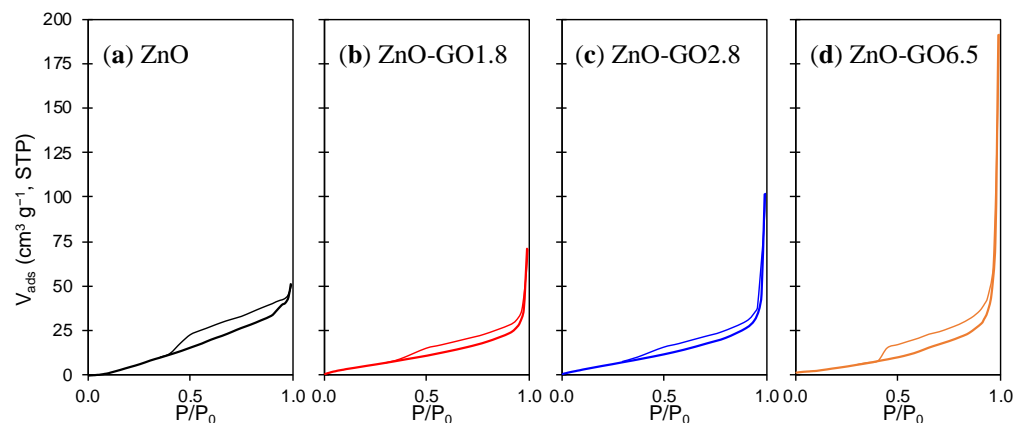


**Figure 2.**  $N_2$  adsorption-desorption isotherms of (a) pristine ZnO, (b) ZnO-GO1.8, (c) ZnO-GO2.8 and (d) ZnO-GO6.5.

Apparent surface areas ( $S_{BET}$ ) of all prepared materials were between 10 and 19  $m^2 g^{-1}$ , with ZnO-GO composites usually presenting higher  $S_{BET}$  than pristine ZnO (e.g., 12 and 18  $m^2 g^{-1}$  for pristine ZnO and ZnO-GO5.5, respectively, Table 1). In general, the addition of GO improved the porosity of the composites, namely the mesopore volume ( $V_{meso}$ ) and the total pore volume ( $V_{total}$ ), these parameters generally increasing as the GO loading increased (e.g.,  $V_{total} = 0.10$  and  $0.29 cm^3 g^{-1}$  for ZnO-GO1.8 and ZnO-GO6.5, respectively).

This improvement in composites' porosity should be attributed to the intercalation of GO layers with ZnO particles generating new interstitial spaces in the mesopore range.

**Table 1.** BET surface area ( $S_{\text{BET}}$ ), mesopore volume ( $V_{\text{meso}}$ ), total pore volume ( $V_{\text{pore}}$ ), pH at the point of zero charge ( $\text{pH}_{\text{PZC}}$ ), band-gap energy ( $E_{\text{g}}$ ) of materials, and crystallite size of synthesized materials.

Samples	$S_{\text{BET}}$ ( $\text{m}^2 \text{g}^{-1}$ )	$V_{\text{meso}}$ ( $\text{cm}^3 \text{g}^{-1}$ )	$V_{\text{total}}$ ( $\text{cm}^3 \text{g}^{-1}$ )	$\text{pH}_{\text{PZC}}$	$E_{\text{g}}$ (eV)	Crystallite Size (nm)
GO	21	n.d.	n.d.	2.8	-	n.d.
ZnO	12	0.07	0.07	7.6	3.12	41
ZnO-GO1.8	19	0.09	0.10	7.4	3.05	36
ZnO-GO2.8	18	0.08	0.09	7.4	3.05	34
ZnO-GO5.5	18	0.13	0.15	7.3	2.98	35
ZnO-GO6.5	10	0.23	0.29	7.3	2.95	35

n.d. = not determined.

The  $\text{pH}_{\text{PZC}}$  for ZnO, GO and the composites are listed in Table 1. The  $\text{pH}_{\text{PZC}}$  value of GO was 2.9, indicating the strong acidic character of the GO surface due to the presence of a large amount of oxygenated groups (mainly epoxy and hydroxyl groups) [69].  $\text{pH}_{\text{PZC}}$  could change depending on the synthesis method and structure of ZnO [70]. In this study, the  $\text{pH}_{\text{PZC}}$  for ZnO was calculated to be approximately 7.6, indicating the neutral/slightly basic character of the semiconductor. The results point out that the  $\text{pH}_{\text{PZC}}$  values for ZnO-GO composites decrease as the GO content increases, resulting in materials with a slightly lower basic character than pristine ZnO [69].

Figure 3a shows the XRD patterns of ZnO nanoparticles and the ZnO-GO composites. The similar patterns obtained denote that the crystalline structure of bare ZnO is maintained in the composites, as reported elsewhere [37,42]. Peaks observed at  $31.9^\circ$ ,  $34.5^\circ$ ,  $36.3^\circ$ ,  $47.6^\circ$ ,  $56.6^\circ$ ,  $62.9^\circ$ ,  $66.5^\circ$ ,  $68.0^\circ$ , and  $69.3^\circ$  correspond to the (100), (002), (101), (102), (110), (103), (200), (112), and (201) planes of the hexagonal ZnO wurtzite structure (JCPDS No. 36-1451), respectively [35,37]. Moreover, the characteristic peak of GO at approximately at  $12^\circ$ , and associated to the reflection for the (001) plane of GO, is not observed in the XRD patterns, due to the low content of GO present in the composites, as well as to the strong diffractions of ZnO that could mask the peak associated to GO [42,44]. The particle size of the ZnO nanoparticles and the ZnO composites were calculated using the Scherrer's equation and the results are included in Table 1. Particles sizes of 41, 36, 34, 35, and 35 nm were calculated for ZnO, ZnO-GO1.8, ZnO-GO2.8, ZnO-GO5.5, and ZnO-GO6.5 photocatalysts, respectively. In general, all the materials showed similar particles size values.

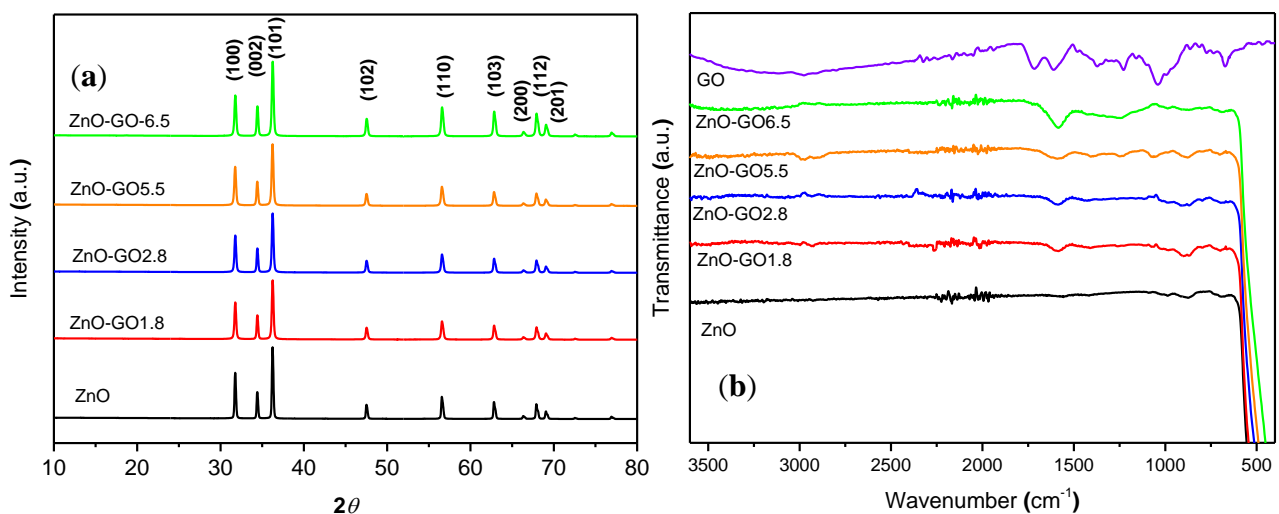


**Figure 3.** (a) XRD patterns of ZnO and ZnO-GO composites, (b) FTIR spectra of GO, ZnO and ZnO-GO composites.

ATR-IR spectra of pristine ZnO, GO and ZnO-GO composites are depicted in Figure 3b. GO spectrum shows the main characteristic bands associated to the presence of oxygen functionalities at around 1050, 1350, and 1720, and a broad band ca. at 3000–3400  $\text{cm}^{-1}$  attributed to C–O, C–OH (stretching), C=O, and C–OH (vibration) groups, respectively [64]. The spectra of ZnO and the composites show a common high intensity band at around 450–500  $\text{cm}^{-1}$ , corresponding to the stretching vibration of Zn–O [71]. In general, the IR-spectra of the ZnO-GO composites also show two weak bands at around 1600  $\text{cm}^{-1}$  and 850  $\text{cm}^{-1}$ , attributed to the bending vibration of water and to the Zn–OH group, respectively [71–73]. It is interesting to note that the intensity of the peaks associated to carbonyl groups (C=O) and epoxy groups (C–O) at around 1700 and 1100  $\text{cm}^{-1}$ , respectively, decreased significantly for the ZnO-GO composites. These results indicate that the anchoring of ZnO to GO could be preferentially through these groups.

The SEM images of ZnO and ZnO-GO1.8, ZnO-GO5.5, and ZnO-GO6.5 are depicted in Figure 4a–f (ZnO and ZnO-GO6.5 are shown for two different magnifications). The ZnO structure consists of rod-like particles with size of ~100 nm and spherical-like particles with ca. 50 nm of diameter (Figure 4a,b). In general, ZnO-GO composites show more aggregated structures in comparison with pristine ZnO, originating larger particle clusters and progressively favouring the formation of flat structures. The formation of ZnO nanoparticles from acetate/nitrate, forming from nanorods to nanoflakes, or grouped forming flower-like structures, depend on the experimental conditions, as previously described [72]. The composite micrographs (Figure 4c–f) do not show GO sheets uncoated with ZnO, indicating a good assembly between ZnO and GO phases for all the composites prepared.

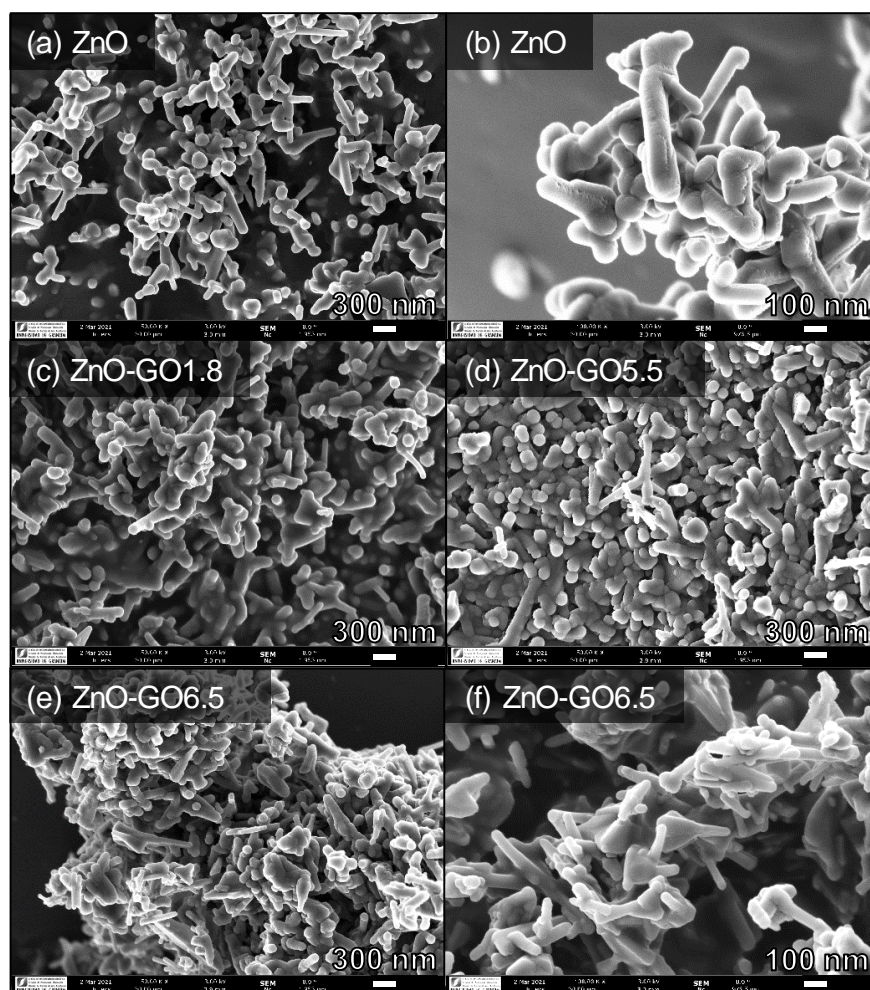
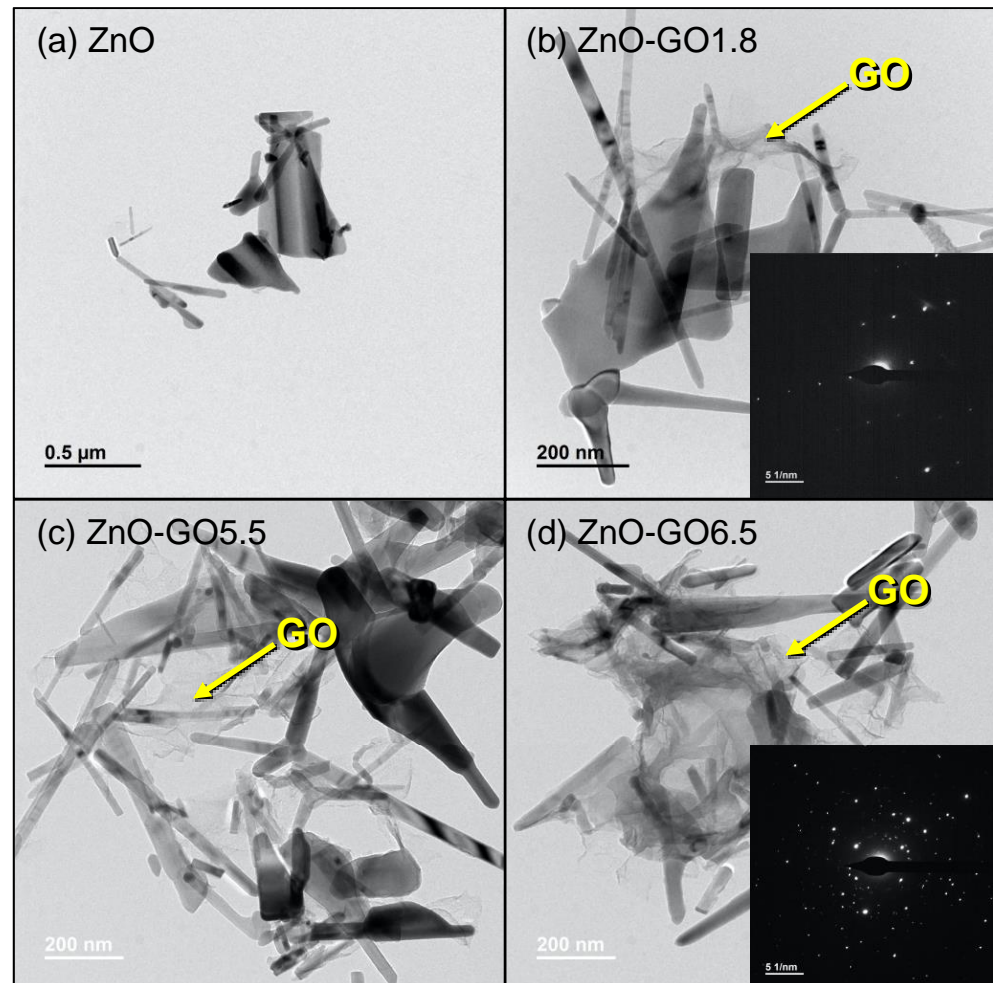


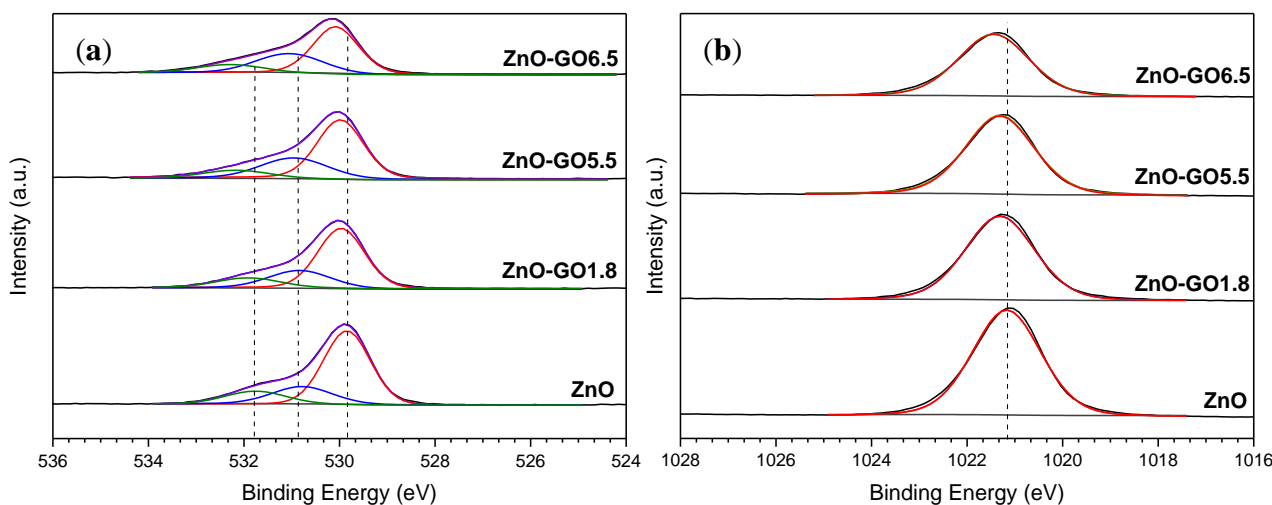
Figure 4. SEM micrographs of (a,b) ZnO, (c) ZnO-GO1.8, (d) ZnO-GO5.5, and (e,f) ZnO-GO6.5.

Figure 5 shows HRTEM images of pristine ZnO and several ZnO-GO composites. In general, ZnO consists of rod-like nanoparticles with a uniform size distribution and clear crystalline structure. Regarding the ZnO-GO composites, micrographs reveal the presence of GO in the composites in the form of aggregated sheet-like structures. The HRTEM images (Figure 5b–d) also show a uniform distribution of the GO between the ZnO structures, inducing a good contact between the two phases. SAED images for selected samples allowed us to corroborate the polycrystalline character of ZnO particles with some of them highly ordered (inset—Figure 5b), and others with several overlapping planes (hkl) corresponding to different nanocrystals (inset—Figure 5d).



**Figure 5.** HRTEM micrographs of (a) ZnO, (b) ZnO-GO1.8, (c) ZnO-GO5.5, and (d) ZnO-GO6.5. Selected areas electron diffraction (SAED) images are included as insets.

The chemical composition of ZnO and the ZnO-GO composites was studied by XPS, the results corresponding to the analysis for the O1s and Zn2p regions shown in Figure 6a,b, respectively. The O1s spectra of the materials were deconvoluted into three components, the first peak placed at ~529.8 eV is assigned to  $O_2^-$  ions from Zn–O bonds belonging to the ZnO wurtzite structure, while the second one at ~530.8 eV corresponds to OH groups absorbed onto the ZnO surface [74], and double-bonded oxygen (C=O) of oxygen-containing groups anchored in the GO structure [75]. The last peak of the O1s region located ~531.8 eV can be ascribed to single-bonded oxygen (C–O) from the oxygen functionalities of GO, in particular alcohol, ether, and epoxy groups [75]. The detected carbon for the ZnO sample could be related to the carbon adsorbed on its surface during the exposure of the sample to the ambient atmosphere [74].



**Figure 6.** XPS spectra and deconvolution of (a) O1s and (b) Zn2p regions of ZnO and selected ZnO-GO composites. (The Zn2p<sub>3/2</sub> region was only represented for clarification).

Regarding the Zn2p region, two peaks were located at  $\sim 1021.2$  and  $\sim 1044.2$  eV, attributed to Zn2p<sub>3/2</sub> and Zn2p<sub>1/2</sub>, respectively, and a binding energy (B.E.) difference of 23.0 eV [74]. The XPS spectra of Zn2p region for the different materials only showed a clear peak at  $\sim 1021.2$  eV, which denotes a Zn<sup>2+</sup> oxidation state. For ZnO-GO composites with larger GO contents, a shifted Zn2p<sub>3/2</sub> peak towards a higher B.E. was observed, due to the chemical environment interaction between ZnO particles and GO functionalities.

UV-Vis diffuse reflectance spectra were carried out in order to determine the electronic properties of pristine ZnO and their composites. For all the photocatalysts, a strong intense absorption band in the UV range with onset at  $< 400$  nm was observed (Figure 7a) This band is associated to the intrinsic band-gap absorption of pristine ZnO [35]. It can be seen that the absorption intensity of the composites is significantly improved in the visible region due to the presence of GO [35,37,44]. In general, this effect is proportional with the different GO loading on the composites, obtaining a stronger absorption capacity in the visible region for the composites with a higher amount of GO (i.e., ZnO-GO5.5 and ZnO-GO6.5). This effect can be attributed to the capacity of carbon materials to absorb light as well as to the creation of electronic interactions between carbon and ZnO as reported in the literature for the case of other carbon and metal oxide phases [38,60,76]. Figure 7b shows the Tauc's plots versus the energy (eV). The calculated  $E_g$  of ZnO, ZnO-GO1.8, ZnO-GO2.8, ZnO-GO5.5, and ZnO-GO6.5 were 3.12, 3.05, 3.05, 2.98, and 2.95 eV, respectively (Table 1), being the obtained band gap for the composites lower than the value obtained for pristine ZnO.

### 3.2. Photocatalytic Activity of the ZnO-GO Composites

The photocatalytic efficiency of ZnO and ZnO-GO composites (with different GO loading) for VA degradation under simulated solar light and visible-LED are shown in Figure 8a,b, respectively. The kinetic rate constant for solar light ( $k_{ap}$ ), the VA conversion ( $X_{VA}$  (%)), and TOC removal ( $X_{TOC}$  (%)) for both solar light and visible-LED are gathered in Table 2. The experiment in the absence of a photocatalyst (i.e., photolysis) shows a null degradation of the contaminant under both solar light (Figure 8a) and visible-LED (not shown). On the other hand, the adsorption equilibrium in dark conditions was established after 60 min for ZnO and ZnO-GO composites, with obtained values of approximately 3–8% of the initial VA concentration. For all the photocatalysts tested, 60 min was proven to be enough to reach the adsorption equilibrium.

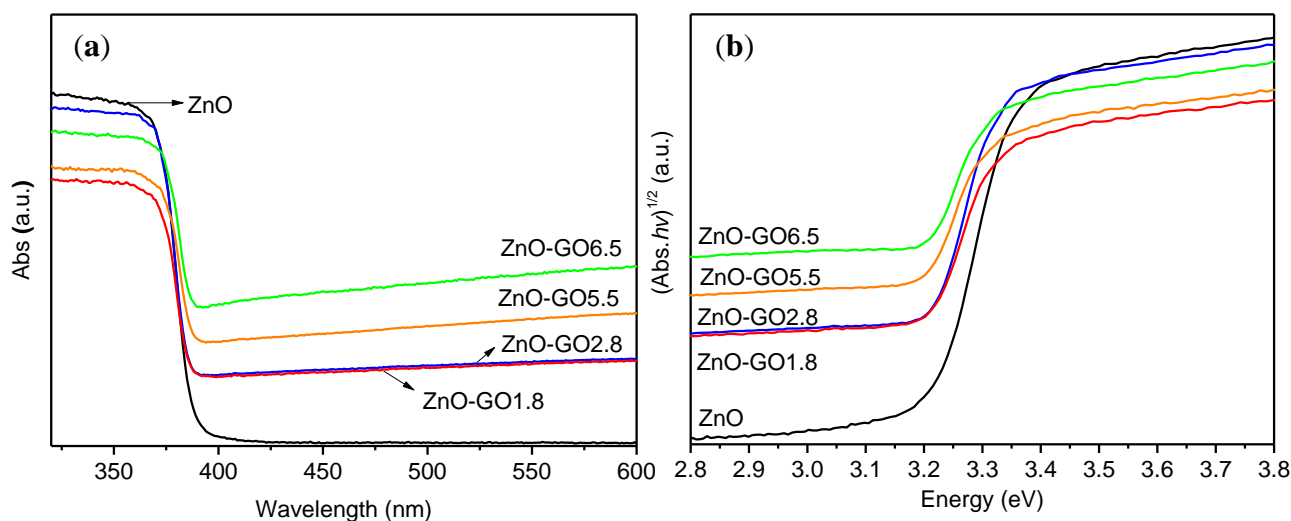


Figure 7. (a) UV-vis spectra and (b) Tauc's plots versus the energy in eV of ZnO and ZnO-GO composites.

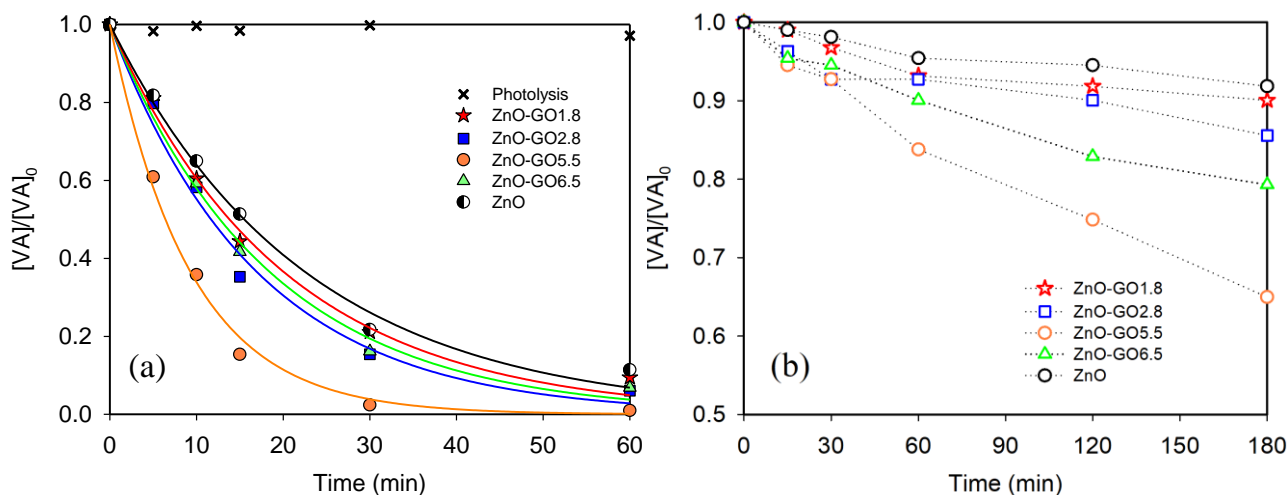


Figure 8. Photocatalytic degradation of VA as a function of time for ZnO and the ZnO-GO composites under (a) simulated solar light and (b) visible-LED.

Table 2. VA conversion ( $X_{VA}$ ), TOC removal (%), pseudo-first order kinetic rate constant ( $k_{ap}$ ), and regression coefficient ( $r^2$ ) under simulated solar light and visible-LED.

Sample	Simulated Solar Light (60 Min)			Visible-LED (180 Min)				
	$X_{VA}$ (%)	$k_{ap}$ ( $10^{-3} \text{ min}^{-1}$ )	$r^2$	$X_{TOC}$ (%)	$X_{TOC}/X_{VA}$	$X_{VA}$ (%)	$X_{TOC}$ (%)	$X_{TOC}/X_{VA}$
Photolysis	2.8	-	-	-	-	-	-	-
ZnO	85.9	$44.7 \pm 2$	0.992	25.9	0.302	8.1	3.2	0.395
ZnO-GO1.8	90.5	$50.2 \pm 2$	0.993	30.5	0.337	9.9	5.5	0.555
ZnO-GO2.8	93.9	$59.4 \pm 4$	0.988	38.9	0.414	14.4	8.1	0.563
ZnO-GO5.5	99.0	$100.8 \pm 5$	0.995	57.5	0.581	35.0	20.1	0.574
ZnO-GO6.5	93.1	$54.6 \pm 3$	0.991	40.2	0.432	20.7	10.7	0.517

Figure 8a shows a significant photocatalytic performance using all the prepared materials for the degradation of VA under solar light. The results indicate that the presence of GO in the composites enhances the degradation efficiency of pristine ZnO under solar light ( $k_{ap} = 100.8 \times 10^{-3} \text{ min}^{-1}$ ,  $59.4 \times 10^{-3} \text{ min}^{-1}$ ,  $54.6 \times 10^{-3} \text{ min}^{-1}$ ,  $50.2 \times 10^{-3} \text{ min}^{-1}$ , and  $44.7 \times 10^{-3} \text{ min}^{-1}$  for ZnO-GO5.5, ZnO-GO2.8, ZnO-GO6.5, ZnO-GO1.8, and ZnO,

respectively). Regarding the results obtained under visible-LED (Figure 8b), a similar trend was observed for VA degradation, i.e., ZnO-GO5.5 (35%) > ZnO-GO6.5 (20.7%) > ZnO-GO2.8 (14.4%) > ZnO-GO1.8 (9.9%) > ZnO (8.1%), where the values in brackets are the VA conversion (Table 2). As expected, the VA degradation under visible-LED was lower than that obtained under simulated solar irradiation as there is no UV irradiation, and only photons with  $\lambda > 430$  nm can reach the samples. For all the photocatalysts tested, the results indicate that the presence of GO enhances the photocatalytic activity under both solar irradiation and visible-LED as previously reported [42,44,77,78]. The possible reasons for higher photocatalytic activity of the ZnO-GO composites compared to pristine ZnO could mainly be ascribed to the increased adsorption capacity, as well as the extended light absorption in the visible range (Figure 7a) [77,78]. Moreover, considering the conduction band of pristine ZnO (c.a.  $-4.05$  eV) [79] and work function of graphene (c.a.  $-4.42$  eV) [80], the direct transfer of photogenerated electrons between ZnO and GO could be favorable. This electron transfer might hinder the electron-hole recombination, enhancing the photocatalytic performance under solar irradiation and visible light as previously observed [78,81].

It is noteworthy that amongst all the prepared materials, the composite containing 5.5 wt.% of GO, i.e., ZnO-GO5.5 exhibits not only the best catalytic activity but also the highest TOC removal in comparison with all other composites under solar irradiation and visible-LED (i.e., 57.5 and 20.1%, respectively, Table 2). These results point out the relevance to select the adequate carbon content in the carbon-semiconductor composites in order to obtain the optimal catalytic performance, as previously reported for other graphene-metal oxide composites [58,60]. However, the lower photocatalytic activity observed for the composite containing a GO loading higher than the optimum value (i.e., ZnO-GO6.5 vs. ZnO-GO5.5) could be associated with the scattering effect of GO [77], or the formation of larger aggregates, as shown by SEM (Figure 4), that could hinder the interactions with the irradiation.

In order to evaluate the mineralization under both solar light and visible-LED, the ratio of TOC removal ( $X_{TOC}$ ) and VA degradation ( $X_{VA}$ ) was introduced in Table 2. In spite of the lower activity obtained under visible-LED compared to solar light (due to the lower extent of the emission spectra), the results show that the experiments under LED illumination were more effective for the mineralization of VA as the ratio ( $X_{TOC}/X_{VA}$ ) was higher under visible-LED than that obtained under simulated solar light (Table 2). It is also noteworthy that this parameter varies according to the tendency previously observed for the photocatalytic activity, i.e., progressively increases with the increases in GO loading but decreases for GO contents higher than the optimum value (i.e., 6.5 wt.%).

### 3.3. Influence of Hole, Radical, and Non-Radical Scavengers and Study of the Stability

The ZnO-GO5.5 composite was selected for a deep study using hole, radical, and non-radical scavengers, in particular ethylenediaminetetraacetic acid (EDTA), methanol (MeOH), and furfuryl alcohol (FFA), respectively, in order to elucidate the possible reactive oxygen species (ROS) involved in the photodegradation of VA under simulated solar light and visible-LED (Figure 9a,b, respectively).

Figure 9a shows the degradation of VA in presence of the selected scavengers under simulated solar irradiation. The results show that all scavengers used decrease the VA degradation. In particular, this effect was more pronounced in the presence of EDTA and to a lesser extent by MeOH and FFA, obtaining a VA degradation of around 5, 81, and 97%, respectively, compared to 99% with no scavenger. These results indicate that, although reactive radicals (formed from photoexcited electrons) and non-radical species (such as singlet oxygen,  $^1O_2$ ) are involved in the reaction, the photogenerated holes seem to be the main responsible species in the degradation of VA (by direct oxidation or by formation of radicals such as  $HO^\bullet$ ) under simulated solar light.

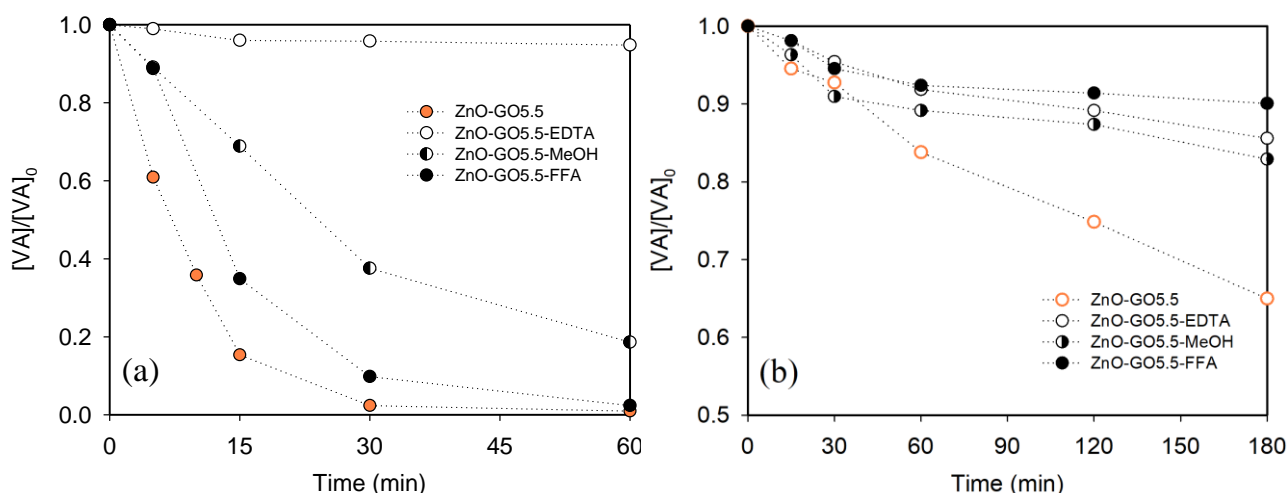


**Figure 9.** Effect of hole/radical/non-radical scavengers (EDTA/MeOH/FFA) on the photocatalytic degradation of VA using ZnO-GO5.5 under (a) simulated solar light and (b) visible-LED.

In the case of visible-LED (Figure 9b), the obtained results also suggest that hole, radical, and non-radical species participate in the reaction mechanism, however, the participation of non-radicals (singlet oxygen,  $^1O_2$ ) in the photocatalytic mechanism seems to play a major representative role in the photocatalytic mechanism under visible-LED, as the degradation observed in presence of FFA was lower in comparison with that obtained for EDTA and MeOH (i.e. 10, 14, and 17%, respectively). The formation of species such as hydroxyl radicals ( $HO^\bullet$ ) and hydroperoxyl radicals ( $HOO^\bullet$ ) under UV irradiation, as well as the formation of other species such as singlet oxygen ( $^1O_2$ ) and superoxide anion ( $O_2^{\bullet-}$ ) under visible light, have been reported in the literature as active species during the degradation of contaminants in the aqueous phase using ZnO and other semiconductors [82–86]. These results show the different photocatalytic mechanisms involved in the degradation of water pollutants under simulated solar irradiation and visible illumination [87].

The photo-stability of photocatalysts is an important factor for industrial applications. Thus, one of the major drawbacks of ZnO is their severe photo-corrosion under UV/Vis irradiation, which can result in a significant decrease in the photocatalytic activity in reused processes [88,89]. Pristine ZnO and ZnO-GO5.5 were selected in order to evaluate its photocatalytic stability in several recycle runs under simulated solar light (i.e., UV-Vis) and visible-LED for 60 min and 180 min, respectively (Figure 10). The experimental procedure was similar to that described in Section 2.3, but in this case after each reaction, the catalyst was rinsed with water and dried in an oven at 80 °C for 5 h before reuse in two additional consecutive photocatalytic experiments. The photocatalytic activity of pristine ZnO decreased during the three consecutive cycles under solar and LED light. However, stability increased in the case of the composite, the conversion values decreasing slightly after the first cycle under both radiations (Figure 10). In fact, the VA conversion ( $X_{VA}$ , %) was lower in the second run in comparison with the first under both simulated solar light (i.e., from 99 to 80%) and visible-LED (i.e., from 35 to 20%), whereas the photocatalytic activity remained practically constant in the third run (75 and 18% for solar light and visible-LED, respectively) for the composite. These results show that the ZnO-GO composite was stable under solar irradiation and visible-LED, indicating that the photo-corrosion of ZnO could be reduced by the presence of GO. This fact highlights the stability and viability of the prepared ZnO-GO composites to work under continuous mode in future studies.

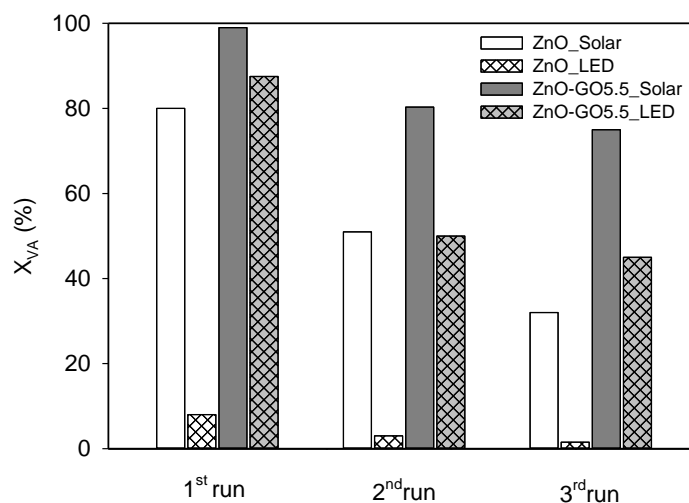


**Figure 10.** Photocatalytic performance of three consecutive cycles degradation for pristine ZnO and ZnO-GO5.5 under simulated solar light and visible-LED.

Table 3 comprises studies regarding different photocatalysts that have been recently published towards phenolic compounds degradation under UV/Vis light irradiation. It can be concluded that the obtained photocatalyst in this work showed a good photocatalytic performance and photostability compared to that of other materials reported in the literature.

**Table 3.** Compilation of recently published works regarding different photocatalysts for phenolic compounds degradation under UV/Vis light irradiation.

Photocatalyst	Contaminant	Light Source	Catalyst Loading (g L <sup>-1</sup> )	Degradation (%)	Ref.
Pd-based photocatalyst	Phenol (20 mg L <sup>-1</sup> )	UV-Vis	0.7	93.75	[90]
TiO <sub>2</sub>	Phenolic compounds (0.53 mM)	UV	1	>90	[91]
Au-ZnO nanomaterials	Phenol, catechol and hydroquinone (25 mg L <sup>-1</sup> )	UV-Vis	1	>85	[92]
Nano-TiO <sub>2</sub>	Phenolic compounds (100 mg L <sup>-1</sup> )	UV	1	97	[93]
rGO-TiO <sub>2</sub>	Phenol, p-chlorophenol and p-nitrophenol (20 mg L <sup>-1</sup> )	UV and Xenon	0.1	~60	[94]
immobilized nano-ZnO	Phenol (2 mg L <sup>-1</sup> )	UV <sub>A</sub>	10–25 m <sup>2</sup> g <sup>-1</sup>	20	[95]
ZnO/TiO <sub>2</sub> -rGO	Phenol (60 mg L <sup>-1</sup> )	3 visible Cd lamps	0.6	100	[96]
ZnO-Graphene	Phenol (40 mg L <sup>-1</sup> )	Solar radiation	1	>90	[97]
ZnO-GO	Vanillic acid (20 mg L <sup>-1</sup> )	Xenon Lamp	1	100	This work
ZnO-GO	Vanillic acid (20 mg L <sup>-1</sup> )	LED visible	1	35	This work

#### 4. Conclusions

Photocatalysts based on ZnO and GO were prepared with different GO contents. The results indicated a high photocatalytic efficiency for the degradation and mineralization of vanillic acid (VA) under simulated solar light and visible-LED ( $\lambda > 430$  nm). SEM images showed that pristine ZnO consisted of rod and spherical-like particles. For the composites, more aggregate structures (with the formation of flat assemblies) were observed. The presence of GO in the composites led to superior photocatalytic performance when compared to that obtained from pristine ZnO under solar light and visible-LED. Nevertheless, the highest catalytic performance was obtained with the composite comprising a GO content of 5.5 wt.%, achieving a VA degradation of 99.0% under simulated solar light. Higher  $X_{TOC}/X_{VA}$  ratios were obtained under LED light, indicating a more efficient mineralization of contaminant in comparison to that obtained under simulated solar light.

The obtained results from the study of hole, radical, and non-radical scavengers suggested that the photogenerated holes seem to be the main responsible species in the degradation of VA under solar light. The participation of singlet oxygen ( $^1\text{O}_2$ ) played a major representative role in the photocatalytic mechanism under visible-LED.

The most effective material, i.e., ZnO-GO5.5, showed better photo-stability in three consecutive runs compared to pristine ZnO, and only a slight decrease of VA degradation was observed under both solar irradiation and visible-LED.

**Author Contributions:** Conceptualization, L.M.P.-M. and S.M.-T.; methodology, N.M., Á.P.-M., F.J.M.-H. and S.M.-T.; investigation, N.M., Á.P.-M., L.M.P.-M. and S.M.-T.; writing—original draft preparation, N.M., Á.P.-M., L.M.P.-M. and A.S.; writing—review and editing, A.S., L.M.P.-M., F.J.M.-H. and S.M.-T.; supervision, F.J.M.-H.; and funding acquisition, L.M.P.-M., S.M.-T. and F.J.M.-H. All authors have read and agreed to the published version of the manuscript.

**Funding:** This work was supported by the Spanish Project ref. RTI 2018-099224-B100 funded by ERDF/Ministry of Science, Innovation and Universities—State Research Agency and the Nano4Fresh project (ref. PCI2020-112045), as part of the PRIMA Programme supported by the European Union.

**Acknowledgments:** Á.P.-M. is grateful to Ministry of Science, Innovation and Universities for a FPI fellowship (ref. PRE2019-087946). L.M.P.-M. (RYC-2016-19347) and S.M.-T. (RYC-2019-026634-I/AEI/10.13039/501100011033) acknowledge the Spanish Ministry of Economy and Competitiveness (MINECO), the State Research Agency and the European Social Found for their Ramón y Cajal research contracts. “Unidad de Excelencia Química Aplicada a Biomedicina y Medioambiente” of the University of Granada (UEQ-UGR) is gratefully acknowledged for the technical assistance. Shahid Beheshti University is appreciated for the partial support of the present study.

**Conflicts of Interest:** The authors declare no conflict of interest.

## References

1. Comninellis, C.; Kapalka, A.; Malato, S.; Parsons, S.A.; Poullos, I.; Mantzavinos, D. Advanced oxidation processes for water treatment: Advances and trends for R&D. *J. Chem. Technol. Biotechnol.* **2008**, *83*, 769–776. [[CrossRef](#)]
2. Priya, B.; Shandilya, P.; Raizada, P.; Thakur, P.; Singh, N.; Singh, P. Photocatalytic mineralization and degradation kinetics of ampicillin and oxytetracycline antibiotics using graphene sand composite and chitosan supported BiOCl. *J. Mol. Catal. A Chem.* **2016**, *423*, 400–413. [[CrossRef](#)]
3. Hussain, S.; Khan, A.J.; Arshad, M.; Javed, M.S.; Ahmad, A.; Shah, S.S.A.; Khan, M.R.; Akram, S.; Zulfiqar, Ali, S.; et al. Charge storage in binder-free 2D-hexagonal CoMoO<sub>4</sub> nanosheets as a redox active material for pseudocapacitors. *Ceram. Int.* **2021**, *47*, 8659–8667. [[CrossRef](#)]
4. Hussain, S.; Yang, X.; Aslam, M.K.; Shaheen, A.; Javed, M.S.; Aslam, N.; Aslam, B.; Liu, G.; Qiao, G. Robust TiN nanoparticles polysulfide anchor for Li-S storage and diffusion pathways using first principle calculations. *Chem. Eng. J.* **2020**, *391*, 123595. [[CrossRef](#)]
5. DeVree, B.T.; Steiner, L.M.; Głazowska, S.; Ruhnnow, F.; Herburger, K.; Persson, S.; Mravec, J. Current and future advances in fluorescence-based visualization of plant cell wall components and cell wall biosynthetic machineries. *Biotechnol. Biofuels* **2021**, *14*. [[CrossRef](#)] [[PubMed](#)]
6. Liu, G.; Zhang, X.; Chen, X.; He, Y.; Cheng, L.; Huo, M.; Yin, J.; Hao, F.; Chen, S.; Wang, P.; et al. Additive manufacturing of structural materials. *Mater. Sci. Eng. R Rep.* **2021**, 100596. [[CrossRef](#)]
7. Eray, E.; Candelario, V.M.; Boffa, V.; Safafar, H.; Østedgaard-Munck, D.N.; Zahrtmann, N.; Kadrispahic, H.; Jørgensen, M.K. A roadmap for the development and applications of silicon carbide membranes for liquid filtration: Recent advancements, challenges, and perspectives. *Chem. Eng. J.* **2021**, *414*. [[CrossRef](#)]
8. Xu, J.; Hong, C.; Geng, J.; Jin, X.; Pan, Y.; Wang, H.; Luo, X.; Zhang, X. Facile synthesis, mechanical toughening, low thermal conductivity and fire-retardant of lightweight quartz fiber reinforced polymer nanocomposites. *Compos. Sci. Technol.* **2021**, *211*. [[CrossRef](#)]
9. Chen, X.; Mao, S.S. Titanium dioxide nanomaterials: Synthesis, properties, modifications and applications. *Chem. Rev.* **2007**, *107*, 2891–2959. [[CrossRef](#)] [[PubMed](#)]
10. Tao, J.; Luttrell, T.; Batzill, M. A two-dimensional phase of TiO<sub>2</sub> with a reduced bandgap. *Nat. Chem.* **2011**, *3*, 296–300. [[CrossRef](#)]
11. Raizada, P.; Kumari, J.; Shandilya, P.; Dhiman, R.; Singh, V.P.; Singh, P. Magnetically retrievable Bi<sub>2</sub>WO<sub>6</sub>/Fe<sub>3</sub>O<sub>4</sub> immobilized on graphene sand composite for investigation of photocatalytic mineralization of oxytetracycline and ampicillin. *Process. Saf. Environ. Prot.* **2017**, *106*, 104–116. [[CrossRef](#)]
12. Pérez-Molina, Á.; Morales-Torres, S.; Maldonado-Hódar, F.J.; Pastrana-Martínez, L.M. Functionalized Graphene Derivatives and TiO<sub>2</sub> for High Visible Light Photodegradation of Azo Dyes. *Nanomaterials* **2020**, *10*, 1106. [[CrossRef](#)]

13. Ong, C.B.; Ng, L.Y.; Mohammad, A.W. A review of ZnO nanoparticles as solar photocatalysts: Synthesis, mechanisms and applications. *Renew. Sustain. Energy Rev.* **2018**, *81*, 536–551. [[CrossRef](#)]
14. Sampaio, M.J.; Lima, M.J.; Baptista, D.L.; Silva, A.M.T.; Silva, C.G.; Faria, J.L. Ag-loaded ZnO materials for photocatalytic water treatment. *Chem. Eng. J.* **2017**, *318*, 95–102. [[CrossRef](#)]
15. McLaren, A.; Valdes-Solis, T.; Li, G.; Tsang, S.C. Shape and Size Effects of ZnO Nanocrystals on Photocatalytic Activity. *J. Am. Chem. Soc.* **2009**, *131*, 12540–12541. [[CrossRef](#)] [[PubMed](#)]
16. Kołodziejczak-Radzimska, A.; Jesionowski, T. Zinc oxide—From synthesis to application: A review. *Materials* **2014**, *7*, 2833–2881. [[CrossRef](#)]
17. Wan, Q.; Li, Q.H.; Chen, Y.J.; Wang, T.-H.; He, X.L.; Li, J.P.; Lin, C.L. Fabrication and ethanol sensing characteristics of ZnO nanowire gas sensors. *Appl. Phys. Lett.* **2004**, *84*, 3654–3656. [[CrossRef](#)]
18. Dai, K.; Lu, L.; Liang, C.; Dai, J.; Zhu, G.; Liu, Z.; Liu, Q.; Zhang, Y. Graphene oxide modified ZnO nanorods hybrid with high reusable photocatalytic activity under UV-LED irradiation. *Mater. Chem. Phys.* **2014**, *143*, 1410–1416. [[CrossRef](#)]
19. Qin, J.; Zhang, X.; Yang, C.; Cao, M.; Ma, M.; Liu, R. ZnO microspheres-reduced graphene oxide nanocomposite for photocatalytic degradation of methylene blue dye. *Appl. Surf. Sci.* **2017**, *392*, 196–203. [[CrossRef](#)]
20. Al-Rawashdeh, N.A.F.; Allabadi, O.; Aljarrah, M.T. Photocatalytic Activity of Graphene Oxide/Zinc Oxide Nanocomposites with Embedded Metal Nanoparticles for the Degradation of Organic Dyes. *ACS Omega* **2020**, *5*, 28046–28055. [[CrossRef](#)]
21. Toporovska, L.; Turko, B.; Savchak, M.; Seyedi, M.; Luzinov, I.; Kostruba, A.; Kapustianyk, V.; Vaskiv, A. Zinc oxide: Reduced graphene oxide nanocomposite film for heterogeneous photocatalysis. *Opt. Quantum Electron.* **2019**, *52*, 21. [[CrossRef](#)]
22. Hoffman, R.L.; Norris, B.J.; Wager, J.F. ZnO-based transparent thin-film transistors. *Appl. Phys. Lett.* **2003**, *82*, 733–735. [[CrossRef](#)]
23. Keis, K.; Magnusson, E.; Lindström, H.; Lindquist, S.-E.; Hagfeldt, A. A 5% efficient photoelectrochemical solar cell based on nanostructured ZnO electrodes. *Sol. Energy Mater. Sol. Cells* **2002**, *73*, 51–58. [[CrossRef](#)]
24. Ahmed, G.; Hanif, M.; Zhao, L.; Hussain, M.; Khan, J.; Liu, Z. Defect engineering of ZnO nanoparticles by graphene oxide leading to enhanced visible light photocatalysis. *J. Mol. Catal. A Chem.* **2016**, *425*, 310–321. [[CrossRef](#)]
25. Kumar, S.G.; Rao, K.S.R.K. Zinc oxide based photocatalysis: Tailoring surface-bulk structure and related interfacial charge carrier dynamics for better environmental applications. *Rsc Adv.* **2015**, *5*, 3306–3351. [[CrossRef](#)]
26. Bizarro, M.; Sánchez-Arzate, A.; Garduno-Wilches, I.; Alonso, J.C.; Ortiz, A. Synthesis and characterization of ZnO and ZnO: Al by spray pyrolysis with high photocatalytic properties. *Catal. Today* **2011**, *166*, 129–134. [[CrossRef](#)]
27. Li, Y.; Della Valle, F.; Simonnet, M.; Yamada, I.; Delaunay, J.-J. Competitive surface effects of oxygen and water on UV photore-sponse of ZnO nanowires. *Appl. Phys. Lett.* **2009**, *94*, 23110. [[CrossRef](#)]
28. Deng, Z.; Chen, M.; Gu, G.; Wu, L. A facile method to fabricate ZnO hollow spheres and their photocatalytic property. *J. Phys. Chem. B* **2008**, *112*, 16–22. [[CrossRef](#)]
29. Lu, F.; Cai, W.; Zhang, Y. ZnO hierarchical micro/nanoarchitectures: Solvothermal synthesis and structurally enhanced photocat-alytic performance. *Adv. Funct. Mater.* **2008**, *18*, 1047–1056. [[CrossRef](#)]
30. Sung, Y.-H.; Frolov, V.D.; Pimenov, S.M.; Wu, J.-J. Investigation of charge transfer in Au nanoparticle–ZnO nanosheet composite photocatalysts. *Phys. Chem. Chem. Phys.* **2012**, *14*, 14492–14494. [[CrossRef](#)]
31. Zheng, Y.; Chen, C.; Zhan, Y.; Lin, X.; Zheng, Q.; Wei, K.; Zhu, J. Photocatalytic activity of Ag/ZnO heterostructure nanocatalyst: Correlation between structure and property. *J. Phys. Chem. C* **2008**, *112*, 10773–10777. [[CrossRef](#)]
32. Kovalenko, A.; Pourroy, G.; Crégut, O.; Gallart, M.; Hönerlage, B.; Gilliot, P. Evidence of unintentional n-doping in ZnO nanorods. *J. Phys. Chem. C* **2010**, *114*, 9498–9502. [[CrossRef](#)]
33. Lin, Y.-G.; Hsu, Y.-K.; Chen, Y.-C.; Chen, L.-C.; Chen, S.-Y.; Chen, K.-H. Visible-light-driven photocatalytic carbon-doped porous ZnO nanoarchitectures for solar water-splitting. *Nanoscale* **2012**, *4*, 6515–6519. [[CrossRef](#)] [[PubMed](#)]
34. Sun, L.-W.; Shi, H.-Q.; Li, W.-N.; Xiao, H.-M.; Fu, S.-Y.; Cao, X.-Z.; Li, Z.-X. Lanthanum-doped ZnO quantum dots with greatly enhanced fluorescent quantum yield. *J. Mater. Chem.* **2012**, *22*, 8221–8227. [[CrossRef](#)]
35. Li, B.; Liu, T.; Wang, Y.; Wang, Z. ZnO/graphene-oxide nanocomposite with remarkably enhanced visible-light-driven photocat-alytic performance. *J. Colloid Interface Sci.* **2012**, *377*, 114–121. [[CrossRef](#)] [[PubMed](#)]
36. Dai, K.; Dawson, G.; Yang, S.; Chen, Z.; Lu, L. Large scale preparing carbon nanotube/zinc oxide hybrid and its application for highly reusable photocatalyst. *Chem. Eng. J.* **2012**, *191*, 571–578. [[CrossRef](#)]
37. Liu, W.M.; Li, J.; Zhang, H.Y. Reduced graphene oxide modified zinc oxide composites synergistic photocatalytic activity under visible light irradiation. *Optik* **2020**, *207*, 163778. [[CrossRef](#)]
38. Sampaio, M.J.; Bacsá, R.R.; Benyounes, A.; Axet, R.; Serp, P.; Silva, C.G.; Silva, A.M.T.; Faria, J.L. Synergistic effect between carbon nanomaterials and ZnO for photocatalytic water decontamination. *J. Catal.* **2015**, *331*, 172–180. [[CrossRef](#)]
39. Johar, M.A.; Afzal, R.A.; Alazba, A.A.; Manzoor, U. Photocatalysis and bandgap engineering using ZnO nanocomposites. *Adv. Mater. Sci. Eng.* **2015**, *2015*. [[CrossRef](#)]
40. Xue, B.; Zou, Y. High photocatalytic activity of ZnO–graphene composite. *J. Colloid Interface Sci.* **2018**, *529*, 306–313. [[CrossRef](#)]
41. Raizada, P.; Sudhaik, A.; Singh, P. Photocatalytic water decontamination using graphene and ZnO coupled photocatalysts: A review. *Mater. Sci. Energy Technol.* **2019**, *2*, 509–525. [[CrossRef](#)]
42. Flores, K.; Valdes, C.; Ramirez, D.; Eubanks, T.M.; Lopez, J.; Hernandez, C.; Alcoutlabi, M.; Parsons, J.G. The effect of hybrid zinc oxide/graphene oxide (ZnO/GO) nano-catalysts on the photocatalytic degradation of simazine. *Chemosphere* **2020**, *259*, 127414. [[CrossRef](#)] [[PubMed](#)]

43. Schelonka, D.; Slušná, M.; Tolasz, J.; Popelková, D.; Ecorchard, P. ZnO-GO Composite with for Photocatalytic Applications. *Mater. Today Proc.* **2016**, *3*, 2679–2687. [[CrossRef](#)]
44. Víctor-Román, S.; García-Bordejé, E.; Hernández-Ferrer, J.; González-Domínguez, J.M.; Ansón-Casaos, A.; Silva, A.M.T.; Maser, W.K.; Benito, A.M. Controlling the surface chemistry of graphene oxide: Key towards efficient ZnO-GO photocatalysts. *Catal. Today* **2020**, *357*, 350–360. [[CrossRef](#)]
45. Morales-Torres, S.; Pastrana-Martínez, L.M.; Figueiredo, J.L.; Faria, J.L.; Silva, A.M.T. Design of graphene-based TiO<sub>2</sub> photocatalysts—A review. *Environ. Sci. Pollut. Res.* **2012**, *19*, 3676–3687. [[CrossRef](#)] [[PubMed](#)]
46. Han, W.; Ren, L.; Qi, X.; Liu, Y.; Wei, X.; Huang, Z.; Zhong, J. Synthesis of CdS/ZnO/graphene composite with high-efficiency photoelectrochemical activities under solar radiation. *Appl. Surf. Sci.* **2014**, *299*, 12–18. [[CrossRef](#)]
47. Li, X.; Wang, Q.; Zhao, Y.; Wu, W.; Chen, J.; Meng, H. Green synthesis and photo-catalytic performances for ZnO-reduced graphene oxide nanocomposites. *J. Colloid Interface Sci.* **2013**, *411*, 69–75. [[CrossRef](#)]
48. Karthik, R.; Thambidurai, S. Synthesis of cobalt doped ZnO/reduced graphene oxide nanorods as active material for heavy metal ions sensor and antibacterial activity. *J. Alloys Compd.* **2017**, *715*, 254–265. [[CrossRef](#)]
49. Zheng, W.T.; Ho, Y.M.; Tian, H.W.; Wen, M.; Qi, J.L.; Li, Y.A. Field emission from a composite of graphene sheets and ZnO nanowires. *J. Phys. Chem. C* **2009**, *113*, 9164–9168. [[CrossRef](#)]
50. Ameen, S.; Akhtar, M.S.; Song, M.; Shin, H.S. Vertically aligned ZnO nanorods on hot filament chemical vapor deposition grown graphene oxide thin film substrate: Solar energy conversion. *ACS Appl. Mater. Interfaces* **2012**, *4*, 4405–4412. [[CrossRef](#)]
51. Lu, Q.; Pan, X.; Wang, W.; Zhou, Y.; Ye, Z. Ultraviolet photodetector based on nanostructured ZnO-reduced graphene oxide composite. *Appl. Phys. A* **2018**, *124*, 733. [[CrossRef](#)]
52. Tien, L.C.; Pearton, S.J.; Norton, D.P.; Ren, F. Synthesis and microstructure of vertically aligned ZnO nanowires grown by high-pressure-assisted pulsed-laser deposition. *J. Mater. Sci.* **2008**, *43*, 6925–6932. [[CrossRef](#)]
53. Pham, C.V.; Repp, S.; Thomann, R.; Krueger, M.; Weber, S.; Erdem, E. Charge transfer and surface defect healing within ZnO nanoparticle decorated graphene hybrid materials. *Nanoscale* **2016**, *8*, 9682–9687. [[CrossRef](#)] [[PubMed](#)]
54. Zhang, Y.; Li, H.; Pan, L.; Lu, T.; Sun, Z. Capacitive behavior of graphene–ZnO composite film for supercapacitors. *J. Electroanal. Chem.* **2009**, *634*, 68–71. [[CrossRef](#)]
55. Wojnarowicz, J.; Chudoba, T.; Lojkowski, W. A Review of Microwave Synthesis of Zinc Oxide Nanomaterials: Reactants, Process Parameters and Morphologies. *Nanomaterials* **2020**, *10*, 1086. [[CrossRef](#)]
56. Hamdi, M. Toxicity and biodegradability of olive mill wastewaters in batch anaerobic digestion. *Appl. Biochem. Biotechnol.* **1992**, *37*, 155–163. [[CrossRef](#)]
57. Hummers, W.S., Jr.; Offeman, R.E. Preparation of graphitic oxide. *J. Am. Chem. Soc.* **1958**, *80*, 1339. [[CrossRef](#)]
58. Pastrana-Martínez, L.M.; Morales-Torres, S.; Likodimos, V.; Figueiredo, J.L.; Faria, J.L.; Falaras, P.; Silva, A.M.T. Advanced nanostructured photocatalysts based on reduced graphene oxide-TiO<sub>2</sub> composites for degradation of diphenhydramine pharmaceutical and methyl orange dye. *Appl. Catal. B Environ.* **2012**, *123–124*, 241–256. [[CrossRef](#)]
59. Tian, C.; Zhang, Q.; Wu, A.; Jiang, M.; Liang, Z.; Jiang, B.; Fu, H. Cost-effective large-scale synthesis of ZnO photocatalyst with excellent performance for dye photodegradation. *Chem. Commun.* **2012**, *48*, 2858–2860. [[CrossRef](#)]
60. Morales-Torres, S.; Pastrana-Martínez, L.M.; Figueiredo, J.L.; Faria, J.L.; Silva, A.M.T. Graphene oxide-P25 photocatalysts for degradation of diphenhydramine pharmaceutical and methyl orange dye. *Appl. Surf. Sci.* **2013**, *275*, 361–368. [[CrossRef](#)]
61. Brunauer, S.; Deming, L.S.; Deming, W.E.; Teller, E. On a Theory of the van der Waals Adsorption of Gases. *J. Am. Chem. Soc.* **1940**, *62*, 1723–1732. [[CrossRef](#)]
62. Sing, K.S.W.; Everett, D.H.; Haul, R.A.W.; Moscou, L.; Pierotti, R.A.; Rouquerol, J.; Siemieniewska, T. Reporting Physisorption Data for Gas/Solid Systems with Special Reference to the Determination of Surface Area and Porosity. *Pure Appl. Chem.* **1985**, *57*, 603–619. [[CrossRef](#)]
63. Barrett, E.P.; Joyner, L.G.; Halenda, P.P. The Determination of Pore Volume and Area Distributions in Porous Substances. I. Computations from Nitrogen Isotherms. *J. Am. Chem. Soc.* **1951**, *73*, 373–380. [[CrossRef](#)]
64. Morales-Torres, S.; Silva, T.L.S.; Pastrana-Martínez, L.M.; Brandão, A.T.S.C.; Figueiredo, J.L.; Silva, A.M.T. Modification of the surface chemistry of single- and multi-walled carbon nanotubes by HNO<sub>3</sub> and H<sub>2</sub>SO<sub>4</sub> hydrothermal oxidation for application in direct contact membrane distillation. *Phys. Chem. Chem. Phys.* **2014**, *16*, 12237–12250. [[CrossRef](#)]
65. Ferro-García, M.A.; Rivera-Utrilla, J.; Bautista-Toledo, I.; Moreno-Castilla, C. Adsorption of Humic Substances on Activated Carbon from Aqueous Solutions and Their Effect on the Removal of Cr(III) Ions. *Langmuir* **1998**, *14*, 1880–1886. [[CrossRef](#)]
66. Newcombe, G.; Hayes, R.; Drikas, M. Granular activated carbon: Importance of surface properties in the adsorption of naturally occurring organics. *Colloids Surf. A Physicochem. Eng. Asp.* **1993**, *78*, 65–71. [[CrossRef](#)]
67. Cullity, B.D.; Stock, S.R. *Elements of X-ray Diffraction*, 3rd ed.; Prentice-Hall: New York, NY, USA, 2001.
68. Zhou, D.; Cheng, Q.-Y.; Han, B.-H. Solvothermal synthesis of homogeneous graphene dispersion with high concentration. *Carbon* **2011**, *49*, 3920–3927. [[CrossRef](#)]
69. Pastrana-Martínez, L.M.; Morales-Torres, S.; Likodimos, V.; Falaras, P.; Figueiredo, J.L.; Faria, J.L.; Silva, A.M.T. Role of oxygen functionalities on the synthesis of photocatalytically active graphene–TiO<sub>2</sub> composites. *Appl. Catal. B Environ.* **2014**, *158–159*, 329–340. [[CrossRef](#)]

70. Zarrabi, M.; Haghghi, M.; Alizadeh, R. Sonoprecipitation dispersion of ZnO nanoparticles over graphene oxide used in photocatalytic degradation of methylene blue in aqueous solution: Influence of irradiation time and power. *Ultrason. Sonochemistry* **2018**, *48*, 370–382. [[CrossRef](#)] [[PubMed](#)]
71. Noei, H.; Qiu, H.; Wang, Y.; Löffler, E.; Wöll, C.; Muhler, M. The identification of hydroxyl groups on ZnO nanoparticles by infrared spectroscopy. *Phys. Chem. Chem. Phys.* **2008**, *10*, 7092–7097. [[CrossRef](#)] [[PubMed](#)]
72. Silva, C.G.; Sampaio, M.J.; Carabineiro, S.A.C.; Oliveira, J.W.L.; Baptista, D.L.; Bacsá, R.; Machado, B.F.; Serp, P.; Figueiredo, J.L.; Silva, A.M.T.; et al. Developing highly active photocatalysts: Gold-loaded ZnO for solar phenol oxidation. *J. Catal.* **2014**, *316*, 182–190. [[CrossRef](#)]
73. Kołodziejczak-Radzimska, A.; Markiewicz, E.; Jesionowski, T. Structural Characterisation of ZnO Particles Obtained by the Emulsion Precipitation Method. *J. Nanomater.* **2012**, *2012*, 656353. [[CrossRef](#)]
74. Al-Gaashani, R.; Radiman, S.; Daud, A.R.; Tabet, N.; Al-Douri, Y. XPS and optical studies of different morphologies of ZnO nanostructures prepared by microwave methods. *Ceram. Int.* **2013**, *39*, 2283–2292. [[CrossRef](#)]
75. Pastrana-Martínez, L.M.; Morales-Torres, S.; Carabineiro, S.A.C.; Buijnsters, J.G.; Figueiredo, J.L.; Silva, A.M.T.; Faria, J.L. Photocatalytic activity of functionalized nanodiamond-TiO<sub>2</sub> composites towards water pollutants degradation under UV/Vis irradiation. *Appl. Surf. Sci.* **2018**, *458*, 839–848. [[CrossRef](#)]
76. Pastrana-Martínez, L.M.; Morales-Torres, S.; Papageorgiou, S.K.; Katsaros, F.K.; Romanos, G.E.; Figueiredo, J.L.; Faria, J.L.; Falaras, P.; Silva, A.M.T. Photocatalytic behaviour of nanocarbon-TiO<sub>2</sub> composites and immobilization into hollow fibres. *Appl. Catal. B Environ.* **2013**, *142–143*, 101–111. [[CrossRef](#)]
77. Zhou, X.; Shi, T.; Zhou, H. Hydrothermal preparation of ZnO-reduced graphene oxide hybrid with high performance in photocatalytic degradation. *Appl. Surf. Sci.* **2012**, *258*, 6204–6211. [[CrossRef](#)]
78. Lv, T.; Pan, L.; Liu, X.; Lu, T.; Zhu, G.; Sun, Z. Enhanced photocatalytic degradation of methylene blue by ZnO-reduced graphene oxide composite synthesized via microwave-assisted reaction. *J. Alloys Compd.* **2011**, *509*, 10086–10091. [[CrossRef](#)]
79. Srikant, V.; Clarke, D.R. On the optical band gap of zinc oxide. *J. Appl. Phys.* **1998**, *83*, 5447–5451. [[CrossRef](#)]
80. Yang, N.; Zhai, J.; Wang, D.; Chen, Y.; Jiang, L. Two-Dimensional Graphene Bridges Enhanced Photoinduced Charge Transport in Dye-Sensitized Solar Cells. *ACS Nano* **2010**, *4*, 887–894. [[CrossRef](#)]
81. Li, B.; Cao, H. ZnO@graphene composite with enhanced performance for the removal of dye from water. *J. Mater. Chem.* **2011**, *21*, 3346–3349. [[CrossRef](#)]
82. Xiang, Q.; Yu, J.; Wong, P.K. Quantitative characterization of hydroxyl radicals produced by various photocatalysts. *J. Colloid Interface Sci.* **2011**, *357*, 163–167. [[CrossRef](#)]
83. Xiao, Q.; Si, Z.; Zhang, J.; Xiao, C.; Tan, X. Photoinduced hydroxyl radical and photocatalytic activity of samarium-doped TiO<sub>2</sub> nanocrystalline. *J. Hazard. Mater.* **2008**, *150*, 62–67. [[CrossRef](#)]
84. Ishibashi, K.-i.; Fujishima, A.; Watanabe, T.; Hashimoto, K. Detection of active oxidative species in TiO<sub>2</sub> photocatalysis using the fluorescence technique. *Electrochem. Commun.* **2000**, *2*, 207–210. [[CrossRef](#)]
85. Banerjee, S.; Pillai, S.C.; Falaras, P.; O’Shea, K.E.; Byrne, J.A.; Dionysiou, D.D. New Insights into the Mechanism of Visible Light Photocatalysis. *J. Phys. Chem. Lett.* **2014**, *5*, 2543–2554. [[CrossRef](#)] [[PubMed](#)]
86. Rengifo-Herrera, J.A.; Pierzchała, K.; Sienkiewicz, A.; Forró, L.; Kiwi, J.; Pulgarin, C. Abatement of organics and Escherichia coli by N, S co-doped TiO<sub>2</sub> under UV and visible light. Implications of the formation of singlet oxygen (<sup>1</sup>O<sub>2</sub>) under visible light. *Appl. Catal. B Environ.* **2009**, *88*, 398–406. [[CrossRef](#)]
87. Cruz, M.; Gomez, C.; Duran-Valle, C.J.; Pastrana-Martínez, L.M.; Faria, J.L.; Silva, A.M.T.; Faraldos, M.; Bahamonde, A. Bare TiO<sub>2</sub> and graphene oxide TiO<sub>2</sub> photocatalysts on the degradation of selected pesticides and influence of the water matrix. *Appl. Surf. Sci.* **2017**, *416*, 1013–1021. [[CrossRef](#)]
88. Fu, H.; Xu, T.; Zhu, S.; Zhu, Y. Photocorrosion inhibition and enhancement of photocatalytic activity for ZnO via hybridization with C60. *Environ. Sci. Technol.* **2008**, *42*, 8064–8069. [[CrossRef](#)]
89. Wang, Y.; Shi, R.; Lin, J.; Zhu, Y. Enhancement of photocurrent and photocatalytic activity of ZnO hybridized with graphite-like C 3 N 4. *Energy Environ. Sci.* **2011**, *4*, 2922–2929. [[CrossRef](#)]
90. Lupa, L.; Coheci, L.; Trica, B.; Coroaba, A.; Popa, A. Photodegradation of Phenolic Compounds from Water in the Presence of a Pd-Containing Exhausted Adsorbent. *Appl. Sci.* **2020**, *10*, 8440. [[CrossRef](#)]
91. Araña, J.; Doña-Rodríguez, J.M.; Portillo-Carrizo, D.; Fernández-Rodríguez, C.; Pérez-Peña, J.; González Díaz, O.; Navío, J.A.; Macías, M. Photocatalytic degradation of phenolic compounds with new TiO<sub>2</sub> catalysts. *Appl. Catal. B Environ.* **2010**, *100*, 346–354. [[CrossRef](#)]
92. Murcia Mesa, J.J.; García Arias, J.A.; Rojas, H.A.; Cárdenas Espinosa, O.E. Photocatalytic degradation of Phenol, Catechol and Hydroquinone over Au-ZnO nanomaterials. *Rev. Fac. Ing. Univ. Antioq.* **2020**, *94*, 24–32. [[CrossRef](#)]
93. Choquette-Labbé, M.; Shewa, W.A.; Lalman, J.A.; Shanmugam, S.R. Photocatalytic Degradation of Phenol and Phenol Derivatives Using a Nano-TiO<sub>2</sub> Catalyst: Integrating Quantitative and Qualitative Factors Using Response Surface Methodology. *Water* **2014**, *6*, 1785–1806. [[CrossRef](#)]
94. Al-Kandari, H.; Abdullah, A.M.; Mohamed, A.M.; Al-Kandari, S. Enhanced photocatalytic degradation of a phenolic compounds’ mixture using a highly efficient TiO<sub>2</sub>/reduced graphene oxide nanocomposite. *J. Mater. Sci.* **2016**, *51*, 8331–8345. [[CrossRef](#)]
95. Tao, Y.; Cheng, Z.L.; Ting, K.E.; Yin, X.J. Photocatalytic Degradation of Phenol Using a Nanocatalyst: The Mechanism and Kinetics. *J. Catal.* **2013**, *2013*, 364275. [[CrossRef](#)]

- 
96. Hayati, F.; Isari, A.A.; Fattahi, M.; Anvaripour, B.; Jorfi, S. Photocatalytic decontamination of phenol and petrochemical wastewater through ZnO/TiO<sub>2</sub> decorated on reduced graphene oxide nanocomposite: Influential operating factors, mechanism, and electrical energy consumption. *RSC Adv.* **2018**, *8*, 40035–40053. [[CrossRef](#)]
  97. Malekshoar, G.; Pal, K.; He, Q.; Yu, A.; Ray, A.K. Enhanced Solar Photocatalytic Degradation of Phenol with Coupled Graphene-Based Titanium Dioxide and Zinc Oxide. *Ind. Eng. Chem. Res.* **2014**, *53*, 18824–18832. [[CrossRef](#)]